INTERNATIONAL JOURNAL FOR NUMERICAL METHODS IN FLUIDS
Int. J. Numer. Meth. Fluids 2003; **41**:951–976 (DOI: 10.1002/fld.475)

A Godunov method for the computation of erosional shallow water transients

L. Fraccarollo[1], H. Capart[2,*,†] and Y. Zech[3]

[1] *Dipartimento di Costruzioni e Tecnologia Avanzata, Università di Messina, and Dipartimento di Ingegneria Civile e Ambientale, Università degli Studi di Trento, Italy*
[2] *Department of Civil Engineering, Université catholique de Louvain, and Fonds National de la Recherche Scientifique, Belgium. Current affiliation: Department of Civil Engineering, National Taiwan University, Taiwan, ROC*
[3] *Department of Civil Engineering, Université catholique de Louvain, Belgium*

SUMMARY

A Godunov method is proposed for the computation of open-channel flows in conditions of rapid bed erosion and intense sediment transport. Generalized shallow water equations govern the evolution of three distinct interfaces: the water free-surface, the boundary between pure water and a sediment transport layer, and the morphodynamic bottom profile. Based on the HLL scheme of Harten, Lax and Van Leer (1983), a finite volume numerical solver is constructed, then extended to second-order accuracy using Strang splitting and MUSCL extrapolation. Lateralisation of the momentum flux is adopted to handle the non-conservative product associated with bottom slope. Computational results for erosional dam-break waves are compared with experimental measurements and semi-analytical Riemann solutions. Copyright © 2003 John Wiley & Sons, Ltd.

KEY WORDS: finite volume; shallow-water equations; sediment transport; erosional dam-break problem

1. INTRODUCTION

Finite volume schemes have matured in recent years into powerful tools for the computation of shallow-water flows over rigid bottom boundaries. Successive developments have produced schemes with good shock-capturing properties [1, 2], second-order accuracy [3, 4], and the ability to deal with irregular bottom profiles [5, 6]. Recent applications have further extended the scope from pure water transients to mudflows and debris surges over non-erodible boundaries [7, 8]. Other computational approaches deal with alluvial channels, in which sediment motion is gentle and the bottom boundary evolves slowly [9, 10]. The present work addresses the case of strong erosional flows, encountered in various conditions of geomorphological and engineering interest. These include valley forming floods [11], debris surges rushing down

*Correspondence to: H. Capart, Department of Civil Engineering and Hydrotech Research Institute, National Taiwan University, 158 Chow-Shan Rd, Taipei 10617, Taiwan, Republic of China.
†E-mail: hcapart@peace.hy.ntu.edu.tw

Received September 2001
Revised 16 October 2002

loose mountainous slopes [12], and sheet-flow sediment transport in the coastal surf and swash zones [13].

For conditions of rapid erosion and intense sediment transport, material entrainment from the bed significantly affects the dynamics of the flow [14]. In particular, both weak and strong shocks may arise as a result of interactions with the bed. Godunov-type schemes are known to deal well with such shocks, hence constitute good candidates to approach the problem. Two difficulties arise, however, which complicate numerical endeavours. First, the formulation of governing equations in a manner both compatible with the flow physics and suitable for computational treatment is not a settled issue [14–16]. Secondly, the quality of computational algorithms has been hard to assess in the absence of reference analytical solutions. Two recent developments partly address these difficulties. The first is the formulation [17] of a set of geomorphic shallow water equations which compares favourably with experiments while keeping a simple mathematical structure. The second is the derivation [18, 19] of a semi-analytical solution which generalises to erosional flows the Stoker solution of shallow water theory [20]. The solution describes the evolution of a dam-break surge released over a loose sediment bed, and provides an appropriate benchmark for the testing of computational algorithms.

Building on the works cited above, the present paper focuses on computational issues. Three main challenges arise in the development of Godunov-type schemes applicable to erosional flows. First, the adopted system of hyperbolic equations features three evolution equations rather than the two equations of classical shallow water theory, and the associated Riemann problems engender a more complex wave structure. This structure is difficult to handle explicitly using field-by-field decomposition [21], hence more diffusive approximate Riemann solvers must be used. To adequately resolve intermediate waves, it becomes important to achieve second-order accuracy. Secondly, the equations involve non-conservative slope effects, a feature which requires adaptation of schemes developed initially for systems of conservation laws [22]. Finally, empirical closures embedded into the equations limit the degree of mathematical detail that one can exploit to construct numerical schemes. These challenges resemble those encountered in gas dynamics when going from simple ideal gas systems to more complex multiphase problems [23, 24]. The computational strategy chosen is based on the HLL solver of Harten, Lax and Van Leer [25]. Lateralization of the momentum flux [26, 27] is adopted to handle the bottom slope in a way suitable for second-order extension of the scheme. The latter is then conducted using Strang splitting [28] and MUSCL extrapolation at the cell faces [29]. The term ‘Lateralized HLL scheme’ or ‘LHLL scheme’ will be used to refer to the proposed method.

The paper proceeds as follows. The physical and mathematical description is introduced in the next section. The proposed LHLL computational scheme is then detailed, and contrasted with an alternative method. The scheme is finally applied to the erosional dam-break problem, for which results are compared with semi-analytical solutions as well as experimental measurements.

2. PHYSICAL AND MATHEMATICAL DESCRIPTION

2.1. Phenomenological assumptions and vertical flow structure

Highly erosive free surface flows propagating over loose beds of coarse, cohesionless sediments are considered. Sediment materials of interest range from the light artificial analogues

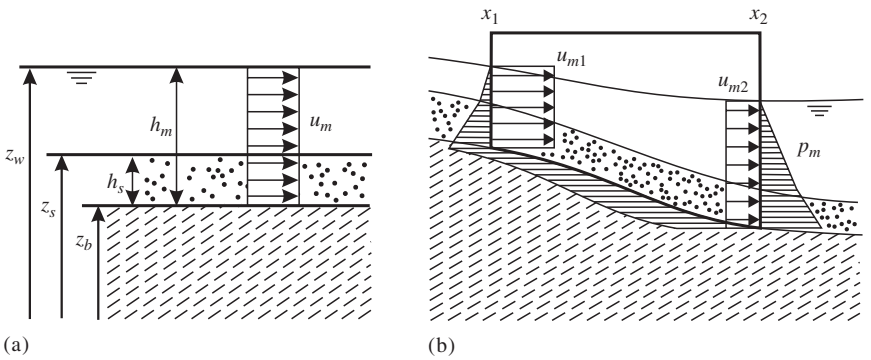

Figure 1. Idealization of the flow: (a) definition sketch showing the layered structure defined by three sharp interfaces; (b) control volume for the derivation of extended shallow water equations.

often used in laboratory studies to the heavier sand, gravel or stone materials found in nature. We focus on regimes of intense erosion and sediment transport, in which coarse sediments are observed to move collectively as a thick layer of contact load. This transport layer can be entrained by an upper layer composed of mostly clear water. It may also invade the entire flow depth, a condition referred to as mature debris flow.

We postulate the vertical flow structure defined by the three sharp interfaces shown on Figure 1(a). Interface z_w is the air–water boundary at the flow free surface. Interface z_s, secondly, defines the upper limit of the sediment transport layer, separating the clear water layer above from the liquid-granular mixture below. The third interface z_b is the bed boundary, and is modelled as a phase interface across which the water–granular mixture undergoes a discontinuous change of state [30]. Above the bed interface z_b, the liquid–granular mixture is assumed to flow as a fluid, while a solid-like behaviour is considered underneath. Erosion occurs as boundary z_b progresses downwards, and deposition results when the boundary moves up. In both cases, no vertical motion of the material takes place: the material simply liquefies or solidifies as it is traversed by the moving interface.

The three interfaces define separate layers for which we adopt the simplest possible distributions of granular concentration and horizontal velocity: piecewise constant vertical profiles. For the granular concentration, first, we assume a sharply stratified profile. Underneath interface z_s, both the transport layer and the static bed are assumed to exhibit the same granular packing $\phi = \phi_s = \phi_b$. In what follows, value $\phi = 0.5$ is retained for both sediment layers. Above interface z_s by contrast, the clear water layer has volumetric solid concentration $\phi = 0$.

A similarly idealized distribution is assumed for the velocity profile. Underneath bed interface z_b, the solid-like bed material is motionless and behaves as a rigid body. Above interface z_b, on the other hand, the entire flow layer moves at horizontal mixture velocity u_m assumed uniform over depth h_m. No slip is thus allowed between the pure water and sediment transport layers. This approximation is expected to be reasonable for fast transients such as the dam-break waves presented in Section 4. For these flows, the driving impulse of the free surface gradient is felt across the flow depth, including both the water and flowing sediment layers. For general flows subject to more prevalent frictional

effects, a two-layer description with separate velocities for the water and sediment transport regions [31–33] would be more appropriate, but lies beyond the scope of the present work.

A shallow water approximation is adopted, in which vertical accelerations are neglected. The hydrostatic assumption then holds in the fluid-like portion of the vertical column. The two fluid-like sub-layers are respectively characterized by densities ρ_w and $\rho_w(1+(s-1)\phi_s) = \rho_w(1+r)$, where $s=\rho_s/\rho_w$ is the density of the sediment material relative to water, and $r=(s-1)\phi_s$ is the density supplement due to the presence of the sediment load. The integral of pressure over the flow depth is thus given by

$$\int_{z_b}^{z_w} p_m \, dz = \rho_w(\tfrac{1}{2} g h_m^2 + \tfrac{1}{2} r g h_s^2) \tag{1}$$

where $h_m = z_w - z_b =$ overall depth of the heterogeneous flowing layer, and $h_s = z_s - z_b =$ depth of the sediment transport sub-layer.

2.2. Governing equations

Governing equations are then derived by invoking continuity and momentum balance principles. Choice of a suitable control volume for momentum balance requires some care, since stresses are defined only in the fluid-like part of the domain. In order for the control surface to enclose fluid-like material exclusively, we fit its lower boundary to the evolving bed interface z_b. This deforming control volume is sketched on Figure 1(b). The set of geomorphic shallow water equations which results is given by References [17, 19]

$$\frac{\partial}{\partial t}(z_b + h_m) + \frac{\partial}{\partial x}(h_m u_m) = 0 \tag{2}$$

$$\frac{\partial}{\partial t}(z_b + h_s) + \frac{\partial}{\partial x}(h_s u_m) = 0 \tag{3}$$

$$\frac{\partial}{\partial t}((h_m + r h_s) u_m) + \frac{\partial}{\partial x}((h_m + r h_s) u_m^2 + \tfrac{1}{2} g h_m^2 + \tfrac{1}{2} r g h_s^2) + g(h_m + r h_s)\frac{\partial z_b}{\partial x} = -\frac{\tau_b}{\rho_w} \tag{4}$$

Equations (2) and (3) are continuity equations enforcing conservation of total volume (water and sediment) and sediment volume, respectively. Equation (4), on the other hand, constitutes a momentum equation for the heterogeneous flowing mixture. The equations take into account the inertia of the eroded material, a feature very important to the description of the flow dynamics in the case of rapid erosional transients. Two further elements are needed to close the equations. First, an empirical function is needed to evaluate the bed shear stress τ_b. Secondly, one must provide either a non-equilibrium evolution equation or an equilibrium transport law for the sediment load h_s. While a non-equilibrium treatment may be needed to describe entrainment of very light granular materials [14], for contact-load transport of natural sediments an equilibrium approximation is usually sufficient [9, 19]. This is the choice adopted in the present work. Laboratory experiments [13, 14, 34] then indicate that the following

simple relations are adequate:

$$\tau_b = \rho_w k h_s \frac{u_m}{|u_m|} \tag{5a}$$

$$h_s = m u_m^2 \tag{5b}$$

where friction factor k and mobility coefficient m are empirical parameters which depend on the relative density of sediment and fluid according to [19]

$$k = \tan\ \varphi\, g(s-1)\phi_s \tag{6a}$$

$$m = \frac{s}{(s-1)\phi_s} \frac{C_f}{\tan\ \varphi\, g} \tag{6b}$$

Under constitutive assumptions (5)–(6), the equations can be made dimensionless by normalizing all lengths by a typical depth h_0, velocity by $c_0 = (gh_0)^{1/2}$, and time by $t_0 = (h_0/g)^{1/2}$. The geomorphic equations thus preserve the Froude similarity of the classical shallow water equations [20] as observed in erosional dambreak experiments [14]. Friction angle φ is a quantity that is well-constrained by available empirical data. The value $\tan\ \varphi = 0.5$ estimated by Nnadi and Wilson [34] is adopted in the present study. Non-dimensional entrainment coefficient C_f, on the other hand, is retained as an adjustable parameter. A calibrated value of $C_f = 0.014$ was obtained by Fraccarollo and Capart [19] for the dam-break experiments described hereafter. If needed, alternative constitutive relations can be incorporated in the present mathematical and computational framework. References [17] and [19] provide more details about the equations, their underlying assumptions, and how they relate to alternative formulations.

Introducing definitions

$$\begin{pmatrix} z_w \\ z_s \\ \pi \end{pmatrix} = \begin{pmatrix} z_b + h_m \\ z_b + h_s \\ (h_m + r h_s) u_m \end{pmatrix} \tag{7a}$$

$$\begin{pmatrix} q_m \\ q_s \\ \sigma \end{pmatrix} = \begin{pmatrix} h_m u_m \\ h_s u_m \\ (h_m + r h_s) u_m^2 + \frac{1}{2} g h_m^2 + \frac{1}{2} r g h_s^2 \end{pmatrix} \tag{7b}$$

the governing Equations (2)–(4) can be rewritten in the more compact form

$$\frac{\partial z_w}{\partial t} + \frac{\partial q_m}{\partial x} = 0 \tag{8}$$

$$\frac{\partial z_s}{\partial t} + \frac{\partial q_s}{\partial x} = 0 \tag{9}$$

$$\frac{\partial \pi}{\partial t} + \frac{\partial \sigma}{\partial x} + g(h_m + r h_s)\frac{\partial z_b}{\partial x} = -\frac{\tau_b}{\rho_w} \tag{10}$$

or, in vector notation

$$\frac{\partial \mathbf{U}}{\partial t} + \frac{\partial \mathbf{F}(\mathbf{U})}{\partial x} + \mathbf{H}(\mathbf{U})\frac{\partial \mathbf{U}}{\partial x} = \mathbf{S}(\mathbf{U}) \tag{11}$$

In the absence of non-conservative product $g(h_m + r h_s)\partial z_b/\partial x$ and source term $-\tau_b/\rho_w$, the equations reduce to standard conservation law form

$$\frac{\partial \mathbf{U}}{\partial t} + \frac{\partial \mathbf{F}}{\partial x} = 0 \tag{12}$$

hence vector $\mathbf{U} = (z_w \; z_s \; \pi)^T$ will be referred as vector of 'conserved variables', and vector $\mathbf{F} = (q_m \; q_s \; \sigma)^T$ interpreted as the corresponding fluxes. Provided one invokes constitutive relation (5b), all components of $\mathbf{U}$ and $\mathbf{F}$ are conveniently expressed in terms of the three components of vector $\mathbf{V} = (h_m \; u_m \; z_b)^T$ which we choose as primitive variables. As source term $-\tau_b/\rho_w$ may be stiff in parts of the flow domain, a point-implicit treatment of this component will be needed but poses no great difficulty [35]. Most importantly, the handling of non-conservative product $g(h_m + r h_s)\partial z_b/\partial x$ associated with bottom slope will require a special computational strategy.

At various steps of the computational scheme, it will be necessary to translate back from conserved variables $\mathbf{U}$ to primitive variables $\mathbf{V}$. Under constitutive assumption (5b), this is easily done algebraically using the Tartaglia-Cardano formula (see e.g. Reference [36])

$$u_m = \sqrt[3]{R + \sqrt{Q^3 + R^2}} + \sqrt[3]{R - \sqrt{Q^3 + R^2}} \text{ in which } Q = \frac{z_w - z_s}{3(1+r)m}, \quad R = \frac{\pi}{2(1+r)m} \tag{13a}$$

$$h_m = z_w - z_s + m u_m^2 \tag{13b}$$

$$z_b = z_s - m u_m^2 \tag{13c}$$

where (13a) is the only physical root of a cubic equation. For different closures, no analytical expressions may be available hence this step would have to be performed numerically.

2.3. Characteristic wave speeds

Using the chain rule, Equations (2)–(4) can be transformed into system

$$\mathbf{B}(\mathbf{V})\frac{\partial \mathbf{V}}{\partial t} + \mathbf{A}(\mathbf{V})\frac{\partial \mathbf{V}}{\partial x} = \mathbf{S}(\mathbf{V}) \tag{14}$$

where

$$\mathbf{A}(\mathbf{V}) = \begin{pmatrix} u_\mathrm{m} & h_\mathrm{m} & 0 \\ 0 & 3h_\mathrm{s} & 0 \\ u_\mathrm{m}^2 + gh_\mathrm{m} & 2(h_\mathrm{m} + (2+gm)rh_\mathrm{s})\,u_\mathrm{m} + & g(h_\mathrm{m} + rh_\mathrm{s}) \end{pmatrix} \tag{15a}$$

$$\mathbf{B}(\mathbf{V}) = \begin{pmatrix} 1 & 0 & 1 \\ 0 & 2mu_\mathrm{m} & 1 \\ u_\mathrm{m} & h_\mathrm{m} + 3rh_\mathrm{s} & 0 \end{pmatrix} \tag{15b}$$

$$\mathbf{S}(\mathbf{V}) = \mathbf{S}(\mathbf{U}(\mathbf{V})) = \begin{pmatrix} 0 \\ 0 \\ -km|u_\mathrm{m}|u_\mathrm{m} \end{pmatrix} \tag{15c}$$

in which $\mathbf{V} = (h_\mathrm{m}\ u_\mathrm{m}\ z_\mathrm{b})^\mathrm{T}$ is the vector of primitive variables, and $\mathbf{A}$ and $\mathbf{B}$ are matrices of coefficients of the x-derivatives and t-derivatives, respectively. Note that non-conservative product $g(h_\mathrm{m} + rh_\mathrm{s})\partial z_\mathrm{b}/\partial x$ is kept within the left hand side divergence operator rather than transferred to the right hand side source term.

Characteristic wavespeeds λ_j are obtained as the generalised eigenvalues of pencil $\mathbf{A} - \lambda\mathbf{B}$ which satisfy [37]

$$\det(\mathbf{A} - \lambda\mathbf{B}) = 0 \tag{16}$$

The resulting cubic polynomial $a_0\lambda^3 + a_1\lambda^2 + a_2\lambda + a_3 = 0$ has coefficients

$$\begin{aligned} &a_0 = h_\mathrm{m} + (2+3r)h_\mathrm{s}, \quad a_1 = -(2h_\mathrm{m} + (5+7r)h_\mathrm{s})u_\mathrm{m} \\ &a_2 = (h_\mathrm{m} + (3+4r)h_\mathrm{s})u_\mathrm{m}^2 - g(h_\mathrm{m}^2 + 2h_\mathrm{s}h_\mathrm{m} + 3rh_\mathrm{s}^2), \quad a_3 = 3(h_\mathrm{m} + rh_\mathrm{s})gh_\mathrm{s}u_\mathrm{m} \end{aligned} \tag{17}$$

and its three roots are given by Reference [36]

$$\lambda_j = 2\sqrt{-Q}\,\cos(\theta_j) - \frac{a_1}{3a_0} \tag{18}$$

where $\theta_1 = \frac{1}{3}\theta + 120°$, $\theta_2 = \frac{1}{3}\theta + 240°$, $\theta_3 = \frac{1}{3}\theta$, and

$$\cos\,\theta = \frac{R}{\sqrt{-Q^3}}, \quad Q = \frac{3a_0a_2 - a_1^2}{9a_0^2}, \quad R = \frac{9a_0a_1a_2 - 27a_0^2a_3 - 2a_1^3}{54a_0^3} \tag{19}$$

In (18), the characteristic speeds are arranged in ascending order $\lambda_1 < \lambda_2 < \lambda_3$. The roots are real and distinct, hence the problem is strictly hyperbolic. By virtue of Froude similarity, the characteristic speeds λ_j can be expressed in the more compact dimensionless form

$$\frac{\lambda_j}{\sqrt{gh_\mathrm{m}}} = \hat{\lambda}_j(Fr, s) \tag{20}$$

where $Fr = u_\mathrm{m}/\sqrt{gh_\mathrm{m}}$ is a local Froude number and $s = \rho_\mathrm{s}/\rho_\mathrm{w}$ is the density contrast. Figure 2 plots this relationship as a function of the Froude number for two different values of

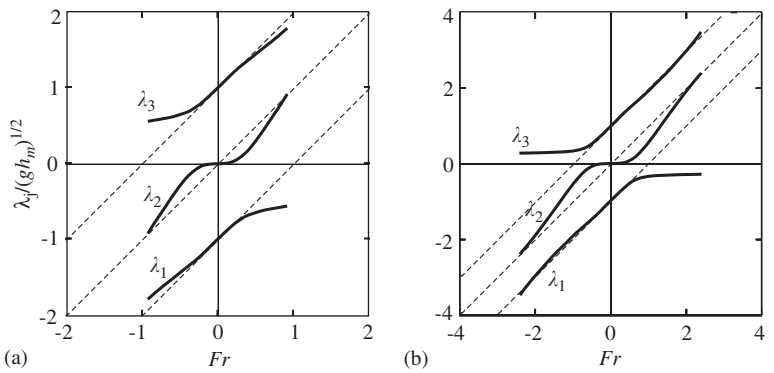

Figure 2. Characteristic wave speeds λ_1, λ_2, and λ_3 given as functions of the local Froude number $Fr = u_m/(gh_m)^{1/2}$ for materials of two different density ratios $s = \rho_s/\rho_w$: (a) $s = 1.05$; (b) $s = 1.5$.

parameter s. Two features of the plots require some comments. First, the eigenvalues are given only on the limited interval

$$-Fr_{\max} \leqslant Fr \leqslant Fr_{\max} \quad \text{where } Fr_{\max} = \frac{1}{\sqrt{mg}} \tag{21}$$

By virtue of constitutive assumption (5b), equality $h_s = h_m$ holds at both limits $Fr = \pm Fr_{\max}$, meaning that the sediment transport layer invades the whole depth of the flow. Constraint (21) is thus equivalent to condition $h_s \leqslant h_m$ which can be understood as follows. Under the present phenomenological assumptions, no seepage flux is allowed between the liquid and granular phases. Starting from initial conditions where the granular medium is everywhere saturated with water (we do not consider the more complex case of partial saturation), it must remain saturated at all subsequent times. States where $h_s > h_m$ are therefore not attainable by the flow, a constraint which is embedded in the governing equations themselves [19]. A second feature which is significant from a computational point of view is that the two outer wavespeeds are confined to opposite half-planes. For non-zero depth $h_m \neq 0$, regardless of the Froude number we have

$$\lambda_1 < 0 < \lambda_3 \tag{22}$$

hence everywhere in the active domain there is at least one wave propagating upstream and one propagating downstream. Both these features are expected to be preserved for reasonable choices of empirical closure relations. The algebra may become less tractable, however, and the corresponding eigenvalues may have to be obtained numerically rather than analytically.

3. COMPUTATIONAL SCHEME

3.1. Basic HLL scheme

Consider first the simpler problem in which non-conservative products and source terms are absent. The equations then reduce to the classical conservation law system (12), which can

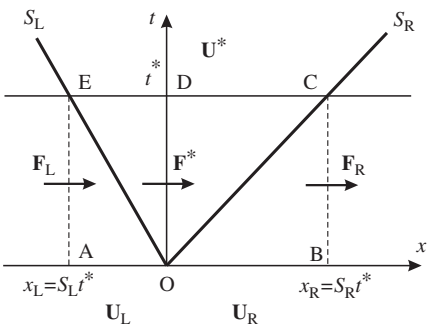

Figure 3. Simplified wave structure adopted for the derivation of flux function $\mathbf{F}^*(\mathbf{U}_L, \mathbf{U}_R)$ in the HLL approach. Only the outer left- and right- going waves having speeds S_L and S_R are retained, and are assumed to bound a central region of constant state $\mathbf{U}^*$.

be integrated along a space-time contour to yield integral equations

$$\oint (\mathbf{U}\,\mathrm{d}x - \mathbf{F}\,\mathrm{d}t) = 0 \tag{23}$$

For a strictly hyperbolic system of equations, Jacobian matrix $\partial\mathbf{F}/\partial\mathbf{U}$ has N real and distinct eigenvalues λ_j which can be given an ordering $\lambda_1 < \cdots < \lambda_N$. First-order accurate computational solutions are constructed by discretising the domain into finite volumes, or cells, featuring piecewise constant states $\mathbf{U}_i$ between positions $x_{i-1/2}$ and $x_{i+1/2}$. The flow is advanced in time from states $\mathbf{U}_i^{(n)}$ at time level $t^{(n)} = n\Delta t$ to states $\mathbf{U}_i^{(n+1)}$ at the next time step using explicit statement

$$\mathbf{U}_i^{(n+1)} = \mathbf{U}_i^{(n)} + \frac{\Delta t}{\Delta x}(\mathbf{F}_{i-1/2}^* - \mathbf{F}_{i+1/2}^*) \tag{24}$$

which represents a discrete version of integral equations (23). In Godunov-type schemes, fluxes $\mathbf{F}_{i+1/2}^*$ are estimated from states $\mathbf{U}_i^{(n)}$, $\mathbf{U}_{i+1}^{(n)}$ to the left and right of each cell face by solving Riemann problem with initial conditions

$$\mathbf{U}(t = t^{(n)}) = \begin{cases} \mathbf{U}_L = \mathbf{U}_i^{(n)} & x < x_{i+1/2} \\ \mathbf{U}_R = \mathbf{U}_{i+1}^{(n)} & x > x_{i+1/2} \end{cases} \tag{25}$$

An approximate Riemann solver with good numerical properties is the well-known HLL scheme proposed by Harten et al. [25] and adapted to shallow water flows in References [3, 38]. Disregarding the details of the wave structure, the approach retains only the extreme left- and right-going waves propagating at speeds S_L, S_R, defining a fan inside which the central state $\mathbf{U}^*$ is assumed uniform in space and constant in time. With reference to Figure 3, integral equations (23) can then be applied to contours AODE and OBCD, respectively, to yield

$$\mathbf{U}^* = \mathbf{U}_L + \frac{\mathbf{F}^* - \mathbf{F}_L}{S_L} \tag{26a}$$

$$\mathbf{U}^* = \mathbf{U}_R + \frac{\mathbf{F}^* - \mathbf{F}_R}{S_R} \tag{26b}$$

Eliminating $\mathbf{U}^*$ between (26a), (26b), one obtains the HLL flux function

$$\mathbf{F}^* = \mathbf{F}^*(\mathbf{U}_\mathrm{L}, \mathbf{U}_\mathrm{R}) = \frac{S_\mathrm{R}\mathbf{F}_\mathrm{L} - S_\mathrm{L}\mathbf{F}_\mathrm{R} + S_\mathrm{L}S_\mathrm{R}(\mathbf{U}_\mathrm{R} - \mathbf{U}_\mathrm{L})}{S_\mathrm{R} - S_\mathrm{L}} \tag{27}$$

Various choices are possible to estimate the wave speeds S_L, S_R [39]. If the outer waves always travel in opposite directions $\lambda_1 < 0 < \lambda_N$, one can simply choose

$$S_\mathrm{L} = \min(\lambda_{1\mathrm{L}}, \lambda_{1\mathrm{R}}) \tag{28a}$$

$$S_\mathrm{R} = \max(\lambda_{N\mathrm{L}}, \lambda_{N\mathrm{R}}) \tag{28b}$$

In the present case, $N = 3$ and the λ_j's are given by Equation (18).

3.2. Continuity equations

Some further adaptations of the HLL scheme are required to treat the geomorphic equations (11). We consider first the homogeneous system in which source term $\mathbf{S}(\mathbf{U})$ is set to zero. The HLL scheme can be directly applied to the first two components of vector $\mathbf{U} = (z_\mathrm{w}\ z_\mathrm{s}\ \pi)^\mathrm{T}$, since their evolution equations (2) and (3) do not involve non-conservative products. We have from (24)

$$(z_\mathrm{w})_i^{(n+1)} = (z_\mathrm{w})_i^{(n)} + \frac{\Delta t}{\Delta x}\left((q_\mathrm{m})_{i-1/2}^* - (q_\mathrm{m})_{i+1/2}^*\right) \tag{29}$$

$$(z_\mathrm{s})_i^{(n+1)} = (z_\mathrm{s})_i^{(n)} + \frac{\Delta t}{\Delta x}\left((q_\mathrm{s})_{i-1/2}^* - (q_\mathrm{s})_{i+1/2}^*\right) \tag{30}$$

where parentheses are used to avoid confusing the different subscripts. Fluxes $(q_\mathrm{m})_{i+1/2}^*$ and $(q_\mathrm{s})_{i+1/2}^*$ can further be estimated directly from (27). For water at rest over a discontinuous step in bottom profile, expression (27) yields $(q_\mathrm{m})_{i+1/2}^* = 0$, as required for water to remain at rest under conditions of hydrostatic balance. As can be verified by substitution, however, expression (27) yields $(q_\mathrm{s})_{i+1/2}^* \neq 0$ which leads to unphysical diffusion of the bottom step. A simple and effective way to prevent this is to invoke inequality $|q_\mathrm{s}| \leqslant |q_\mathrm{m}|$ implied by constraint (21) and set

$$(q_\mathrm{s})_{i+1/2}^* = \mathrm{minmod}((q_\mathrm{s})_{i+1/2}^*, (q_\mathrm{m})_{i+1/2}^*) \tag{31}$$

where the minmod function is defined as

$$\mathrm{minmod}(a,b) = \begin{cases} a & \text{if } |a| \leqslant |b| \text{ and } ab > 0 \\ b & \text{if } |b| < |a| \text{ and } ab > 0 \\ 0 & \text{if } ab \leqslant 0 \end{cases} \tag{32}$$

3.3. Lateralized momentum flux

Evolution equation (4) for the momentum density, on the other hand, involves non-conservative product $g(h_\mathrm{m} + rh_\mathrm{s})\partial z_\mathrm{b}/\partial x$ associated with bottom slope. Rather than treat this term as

a source, we adopt an approach inspired from References [26, 27] based on the following 'lateralized' version of statement (24):

$$\pi_i^{(n+1)} = \pi_i^{(n)} + \frac{\Delta t}{\Delta x}(\sigma_{i-1/2}^{*\mathrm{R}} - \sigma_{i+1/2}^{*\mathrm{L}}) \tag{33}$$

where

$$\sigma_{i+1/2}^{*\mathrm{L}} - \sigma_{i+1/2}^{*\mathrm{R}} = g\langle h_\mathrm{m} + rh_\mathrm{s}\rangle_{i+1/2}^{(n)}((z_\mathrm{b})_{i+1}^{(n)} - (z_\mathrm{b})_i^{(n)}) \tag{34}$$

and $\langle h_\mathrm{m} + rh_\mathrm{s}\rangle_{i+1/2}^{(n)}$ denotes an arithmetic average between left and right values:

$$\langle h_\mathrm{m} + rh_\mathrm{s}\rangle_{i+1/2}^{(n)} = \tfrac{1}{2}((h_\mathrm{m} + rh_\mathrm{s})_i^{(n)} + (h_\mathrm{m} + rh_\mathrm{s})_{i+1}^{(n)}) \tag{35}$$

In essence, we introduce the effect of the non-conservative product as a correction to the numerical flux function $\sigma_{i+1/2}^*$ which makes it double-valued. The momentum flux $\sigma_{i+1/2}^{*\mathrm{R}}$ flowing into the right cell $i+1$ becomes distinct from the momentum flux $\sigma_{i+1/2}^{*\mathrm{L}}$ flowing out of the left cell i, hence the term 'flux lateralisation'. The difference between the two values accounts for the effect of the non-conservative product. Consistent with the non-conservative nature of this term, momentum is injected into or drained from the flow as a result. The advantage of such a treatment will become most apparent when we extend the scheme to second-order accuracy. For now, we apply the basic HLL approach to this modified problem and evaluate

$$\pi^* = \pi_\mathrm{L} + \frac{\sigma^{*\mathrm{L}} - \sigma_\mathrm{L}}{S_\mathrm{L}} \tag{36a}$$

$$\pi^* = \pi_\mathrm{R} + \frac{\sigma^{*\mathrm{R}} - \sigma_\mathrm{R}}{S_\mathrm{R}} \tag{36b}$$

which are counterparts to expressions (26a), (26b). Eliminating π^* between (36a) and (36b), and invoking (34), one obtains for the lateralized momentum fluxes

$$\sigma^{*\mathrm{L}} = \sigma^* - \frac{S_\mathrm{L}}{S_\mathrm{R} - S_\mathrm{L}}\frac{g}{2}((h_\mathrm{m} + rh_\mathrm{s})_\mathrm{L} + (h_\mathrm{m} + rh_\mathrm{s})_\mathrm{R})((z_\mathrm{b})_\mathrm{R} - (z_\mathrm{b})_\mathrm{L}) \tag{37}$$

$$\sigma^{*\mathrm{R}} = \sigma^* - \frac{S_\mathrm{R}}{S_\mathrm{R} - S_\mathrm{L}}\frac{g}{2}((h_\mathrm{m} + rh_\mathrm{s})_\mathrm{L} + (h_\mathrm{m} + rh_\mathrm{s})_\mathrm{R})((z_\mathrm{b})_\mathrm{R} - (z_\mathrm{b})_\mathrm{L}) \tag{38}$$

in which σ^* is given by the unmodified HLL flux function (27). The non-conservative term thus influences the numerical fluxes in two ways: first, it is included in the divergence operator on the basis of which characteristic speeds are evaluated; secondly, it leads to a double-valued correction of the momentum flux. Thanks to the choice of average (35), it can be verified that the compatibility condition of Nujic [6] is met by the present scheme. For water at rest with a horizontal free-surface, the hydrostatic pressures applied along the faces and bottom of a cell will balance exactly regardless of the underlying topography variations. This is required to insure a good behaviour of the scheme when the bottom profile is irregular.

3.4. Frictional source term

The source term $\mathbf{S}(\mathbf{U})$ remains to be incorporated in the procedure. Using Strang splitting [28, 39], one complete time-marching iteration is performed by application of the two successive statements

$$\mathbf{U}_i^{(n+1/2)} = \mathbf{U}_i^{(n)} + \frac{\Delta t}{\Delta x}(\mathbf{F}_{i-1/2}^{*\mathrm{R}} - \mathbf{F}_{i+1/2}^{*\mathrm{L}}) \tag{39a}$$

$$\mathbf{U}_i^{(n+1)} = \mathbf{U}_i^{(n+1/2)} + \Delta t \mathbf{S}(\mathbf{U}_i^{(n+1)}) \tag{39b}$$

where the first step (39a) is the partially lateralised hyperbolic operator defined above and the second step (39b) integrates the source term. It is again to be stressed that the non-conservative bottom slope effect is included in the hyperbolic operator of the first step rather than as part of the source term, which includes only frictional momentum loss. Integration of the latter is carried out in (39b) using an implicit backward Euler scheme in order to guarantee stability regardless of the source strength [35]. Since only the momentum equation component of $\mathbf{S}(\mathbf{U})$ is non-zero, (39b) reduces to

$$(z_\mathrm{w})_i^{(n+1)} = (z_\mathrm{w})_i^{(n+1/2)} \tag{40a}$$

$$(z_\mathrm{s})_i^{(n+1)} = (z_\mathrm{s})_i^{(n+1/2)} \tag{40b}$$

$$\pi_i^{(n+1)} = \pi_i^{(n+1/2)} - \Delta t \frac{(\tau_\mathrm{b})_i^{(n+1)}}{\rho_\mathrm{w}} \tag{40c}$$

or, invoking constitutive relations (5),

$$\begin{aligned}&((z_\mathrm{w})_i^{(n+1/2)} - (z_\mathrm{s})_i^{(n+1/2)} + (1+r)m(u_\mathrm{m})_i^{(n+1)^2})(u_\mathrm{m})_i^{(n+1)} \\ &\quad = \pi_i^{(n+1/2)} - \Delta t k m |(u_\mathrm{m})_i^{(n+1)}|(u_\mathrm{m})_i^{(n+1)}\end{aligned} \tag{41}$$

which reduces to a cubic equation in the single unknown $(u_\mathrm{m})_i^{(n+1)}$. The sole physical root is easily isolated, allowing direct evaluation of the momentum density at the next time level $\pi_i^{(n+1)}$.

3.5. Extension to second-order accuracy

Extension to second order accuracy is carried out as follows. Second order accuracy in space is based on the MUSCL approach proposed by Van Leer [29] and applied in References [4, 6] to the classical shallow water equations. Rather than piecewise constant states within each of the computational cells, piecewise linear states are assumed (see Figure 4). Gradients $\delta\mathbf{U}_i$ of the variables within each cell are estimated from local values of $\mathbf{U}$ using the minmod slope limiter

$$\delta\mathbf{U}_i = \mathrm{minmod}(\mathbf{U}_{i+1} - \mathbf{U}_i, \mathbf{U}_i - \mathbf{U}_{i-1}) \tag{42}$$

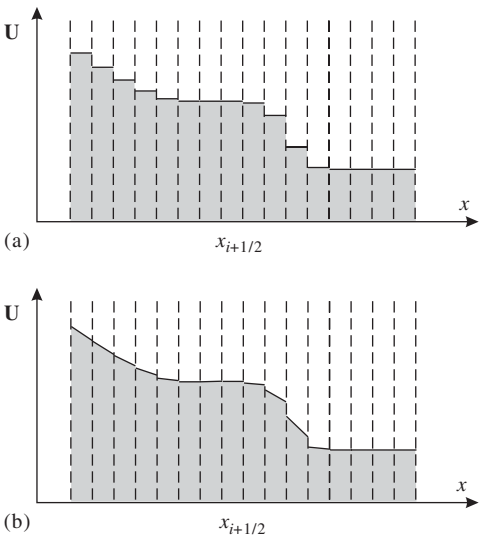

Figure 4. Spatial variations of state variables $\mathbf{U}(x)$ assumed in the first-order and second-order accurate versions of the scheme: (a) piecewise constant states; (b) piecewise linear states with gradients subject to the minmod slope limiter (MUSCL).

where the minmod function is defined as in (32). States $\mathbf{U}^{\mathrm{L}}$ and $\mathbf{U}^{\mathrm{R}}$ to the left and right of a given interface $i+1/2$ are then be obtained by extrapolation as

$$\mathbf{U}^{\mathrm{L}}_{i+1/2} = \mathbf{U}_i + \tfrac{1}{2}\delta\mathbf{U}_i \tag{43a}$$

$$\mathbf{U}^{\mathrm{R}}_{i+1/2} = \mathbf{U}_{i+1} - \tfrac{1}{2}\delta\mathbf{U}_{i+1} \tag{43b}$$

and provide left and right states appropriate for approximate Riemann solvers such as the HLL scheme described above.

Second order accuracy in time is obtained by decomposing the time marching iteration into the following four steps:

$$\mathbf{U}_i^{(n+1/4)} = \mathbf{U}_i^{(n)} + \frac{\Delta t}{2}\mathbf{S}(\mathbf{U}_i^{(n+1/4)}) \tag{44a}$$

$$\mathbf{U}_i^{(n+1/2)} = \mathbf{U}_i^{(n+1/4)} + \frac{\Delta t}{2\Delta x}(\mathbf{F}^{*\mathrm{R}(n+1/4)}_{i-1/2} - \mathbf{F}^{*\mathrm{L}(n+1/4)}_{i+1/2}) - \frac{\Delta t}{2\Delta x}\mathbf{H}_i^{(n+1/4)}\delta\mathbf{U}_i^{(n+1/4)} \tag{44b}$$

$$\mathbf{U}_i^{(n+3/4)} = \mathbf{U}_i^{(n+1/4)} + \frac{\Delta t}{\Delta x}(\mathbf{F}^{*\mathrm{R}(n+1/2)}_{i-1/2} - \mathbf{F}^{*\mathrm{L}(n+1/2)}_{i+1/2}) - \frac{\Delta t}{\Delta x}\mathbf{H}_i^{(n+1/2)}\delta\mathbf{U}_i^{(n+1/4)} \tag{44c}$$

$$\mathbf{U}_i^{(n+1)} = \mathbf{U}_i^{(n+3/4)} + \frac{\Delta t}{2}\mathbf{S}(\mathbf{U}_i^{(n+1)}) \tag{44d}$$

The outer steps (44a) and (44d) integrate the source term [23], while the inner steps (44b) and (44c) correspond to a predictor–corrector procedure for the hyperbolic operator [4]. Together, the four steps constitute a second order version of the Strang splitting procedure of equations (39a), (39b). The outer implicit steps (44a) and (44d) are carried out in exactly the same way as before. For the inner steps (44b) and (44c), on the other hand,

$$\mathbf{F}_{i+1/2}^{*\mathrm{L,R}(n+1/4)} = \mathbf{F}_{i+1/2}^{*\mathrm{L,R}}(\mathbf{U}_{i+1/2}^{L(n+1/4)}, \mathbf{U}_{i+1/2}^{R(n+1/4)}) \tag{45a}$$

$$\mathbf{F}_{i+1/2}^{*\mathrm{L,R}(n+1/2)} = \mathbf{F}_{i+1/2}^{*\mathrm{L,R}}(\mathbf{U}_{i+1/2}^{L(n+1/2)}, \mathbf{U}_{i+1/2}^{R(n+1/2)}) \tag{45b}$$

where functions $\mathbf{F}^{*\mathrm{L}}$ and $\mathbf{F}^{*\mathrm{R}}$ are the lateralized HLL flux functions defined in the previous section, and the $\mathbf{U}^{\mathrm{L}}$, $\mathbf{U}^{\mathrm{R}}$ are obtained from (43) as

$$\mathbf{U}_{i+1/2}^{\mathrm{L}(n+1/4)} = \mathbf{U}_{i}^{(n+1/4)} + \tfrac{1}{2}\delta\mathbf{U}_{i}^{(n+1/4)}, \quad \mathbf{U}_{i+1/2}^{\mathrm{R}(n+1/4)} = \mathbf{U}_{i+1}^{(n+1/4)} - \tfrac{1}{2}\delta\mathbf{U}_{i+1}^{(n+1/4)} \tag{46a}$$

$$\mathbf{U}_{i+1/2}^{\mathrm{L}(n+1/2)} = \mathbf{U}_{i}^{(n+1/2)} + \tfrac{1}{2}\delta\mathbf{U}_{i}^{(n+1/4)}, \quad \mathbf{U}_{i+1/2}^{\mathrm{R}(n+1/2)} = \mathbf{U}_{i+1}^{(n+1/2)} - \tfrac{1}{2}\delta\mathbf{U}_{i+1}^{(n+1/4)} \tag{46b}$$

Notice in (44c) and (46b) that the slopes $\delta\mathbf{U}_i$ are not recomputed at step $n+1/2$ but simply carried over from step $n+1/4$ [4]. The novel aspect of the present formulation lies in the treatment of non-conservative product $\mathbf{H}\partial\mathbf{U}/\partial x$ standing for bottom slope term $g(h_{\mathrm{m}} + rh_{\mathrm{s}})\partial z_{\mathrm{b}}/\partial x$. The bottom profile variations are decomposed into two distinct parts: continuous bottom variations inside each of the computational cells, first, and secondly discontinuous steps at each of the cell faces. The former are accounted for in a classical fashion by the last term on the right hand sides of (44b) and (44c). The latter are accounted for by the differences between the two lateralised values of the momentum flux $\sigma_{i+1/2}^{*\mathrm{L}}$, $\sigma_{i+1/2}^{*\mathrm{R}}$ at each of the cell faces. As was the case for the first order scheme, it can be verified that exact hydrostatic balance is satisfied regardless of bottom variations for water at rest with a horizontal free-surface. Extension from first order to second order accuracy comes at no significant additional expense, and will turn out to yield substantial improvements for the benchmark case examined in the next section.

As the source operator is treated in a point-implicit fashion, the stability of the scheme depends on the explicit hyperbolic operator [35]. For both the first and second order versions of the scheme, the usual Courant condition must hold, i.e.

$$Cr = \frac{\Delta t}{\Delta x} \max_i (\lambda_{\max})_i \leqslant 1 \quad \text{where } \lambda_{\max} = \max(-\lambda_1, \lambda_3) \tag{47}$$

and the λ_j's are the characteristic wave speeds given by Equation (18). For the Courant number Cr, value $Cr = 0.95$ is adopted in all the computations reported hereafter. Although a rigorous stability analysis underpinning criterion (47) was not performed, the condition was verified in practice to lead to well-behaved computations. Similar stability guidelines have been proposed for the computation of pure water flows subject to the effects of slope, friction and infiltration [35, 40].

3.6. *Alternative CLF method*

For comparison purposes, we have also implemented an alternative Godunov method which adapts to the erosional case the scheme proposed by Nujic [6] for shallow water flow over

an irregular rigid bottom. It is similar to a method applied by Saurel and Abgrall [24] to multiphase shock-tube problems, and differs from the present method in two regards. First, a simpler Lax–Friedrichs flux function is used instead of the HLL function (27), i.e.

$$\mathbf{F}^*(\mathbf{U}_L, \mathbf{U}_R) = \tfrac{1}{2}(\mathbf{F}_L + \mathbf{F}_R) - \tfrac{1}{2}S(\mathbf{U}_R - \mathbf{U}_L) \tag{48}$$

where $S = \max|\lambda_j|$ i.e. the eigenvalue of largest magnitude. Secondly, the pressure $p = \frac{1}{2}gh_m^2 + \frac{1}{2}rgh_s^2$ is extracted from the momentum flux, and its gradient treated jointly with bottom slope by central differences. The momentum flux thus reduces to the convected inertia component $\sigma = (h_m + rh_s)u_m^2$, and is evaluated at cell faces using flux function (48). The time-marching step for momentum density, on the other hand, becomes

$$\pi_i^{(n+1)} = \pi_i^{(n)} + \frac{\Delta t}{\Delta x}(\sigma^*_{i-1/2} - \sigma^*_{i+1/2}) + \frac{\Delta t}{2\Delta x}(p_{i-1}^{(n)} - p_{i+1}^{(n)}) + \frac{\Delta t}{4\Delta x}((h_m + rh_s)_{i-1}^{(n)} + (h_m + rh_s)_{i+1}^{(n)})((z_b)_{i-1}^{(n)} - (z_b)_{i+1}^{(n)}) \tag{49}$$

in which the pressure and bottom slope terms are discretised in a way which guarantees exact hydrostatic balance for water at rest with a horizontal free surface. To allow comparison, all other details are identical with the present LHLL implementation. We will refer to this alternative method as 'Centred Lax-Friedrichs' or CLF scheme, since it centres the treatment of fluxes, pressure gradients, and slope. This is a strategy exactly opposite to the present lateralised treatment, which bundles the bottom slope with the pressure thrust in the momentum flux function. To extend the CLF scheme to second-order, Nujic [6] also used MUSCL extrapolation. Like the present treatment, his scheme was designed to preserve oscillation-free properties despite the presence of a non-conservative product.

4. EROSIONAL DAM-BREAK WAVE APPLICATION

4.1. Experimental data and semi-analytical benchmark solution

The proposed Godunov scheme can now be applied to the erosional dam-break problem illustrated on Figure 5. Initially, a body of water at rest is retained upstream of an idealised dam, with a horizontal erodible bed channel extending on both sides. The bed is composed of loose granular material saturated with water. The dam is removed at time $t = 0$, releasing a water surge which entrains material from the bed and rapidly evolves into a heterogeneous liquid-granular flow. The idealised initial conditions are sketched on Figure 5(a), while Figure 5(b) depicts a surge observed experimentally moments after release of a sluice gate.

Laboratory experiments featuring erosional transients of this kind are reported in References [14, 17, 19]. The experiments were carried out in Taipei (National Taiwan University) and Louvain-la-Neuve (Université catholique de Louvain) with coarse granular materials of two different densities. Light material characterised by density ratio $s = \rho_s/\rho_w = 1.048$ was used in the Taipei experiments, while material of intermediate density $s = 1.54$ was used in the Louvain tests. Sediment analogues which are lighter than natural sediments (for which $s \approx 2.65$) are chosen in both cases in order to magnify the phenomena and facilitate observations. The experimental flows were filmed from the side using high-speed CCD cameras.

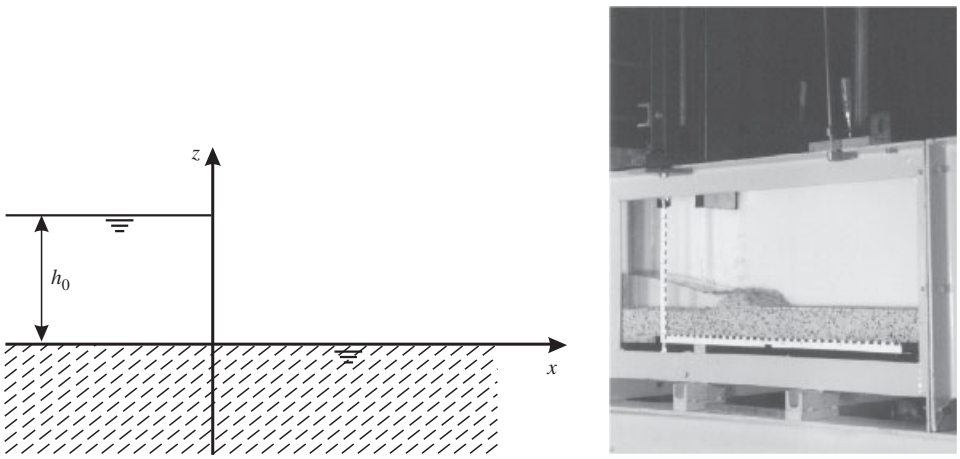

Figure 5. Erosional dam-break problem: (a) initial conditions with idealised dam; (b) view of a laboratory test moments after release of the sluice gate representing the dam (photograph courtesy of J.-L. Van Goethem and L. Villers).

Images were then analysed using Particle Tracking Techniques in order to pick up individual grain motion and characterize the granular velocity field in the 2D vertical plane. Finally, profiles were obtained for the three evolving interfaces z_w, z_s, and z_b on the basis of the digital images and granular velocity fields. The latter are needed to identify the morphodynamic boundary z_b between the static granular bed and the flowing granular dispersion. The procedure and results are fully documented in References [14, 19] and only the final interface measurements are used below for comparison purposes.

In Reference [41], some of the modelling hypotheses were scrutinized further on the basis of dam-break tests performed with sediment material of intermediate density ($s = 1.54$). In that work, measurements were obtained by tracking both the sediment particles and a set of buoyant tracers floating on the water free surface. Beyond the first instants following the raising of the gate (after non-dimensional time $t_0 \approx 1$), vertical accelerations were checked to be small throughout the flow. The choice of a uniform velocity profile over the flow depth was also found to be a reasonable approximation: in the central region of the wave (around position $x = 0$), the velocity of the floating tracers along the water free surface z_w was no more than 30% in excess of the particle velocity at the top of the sediment transport layer z_s. Sharp stratification into particle-free and particle-rich layers of the flow was also verified.

The idealized erosional dam-break flow constitutes a Riemann problem similar to the shock-tube problem of gas dynamics and the dam-break problem of pure water hydrodynamics. Provided one neglects source term $\mathbf{S}(\mathbf{U})$ on the right hand side of Equations (11), the system reduces to a homogeneous set of hyperbolic equations. This amounts to neglecting the momentum loss $-\tau_b/\rho_w$ due to bed friction. As can be demonstrated by a time scale analysis [19], this approximation is justified for the first stages of the erosional wave development. In that case, it is shown in Reference [19] how Riemann solutions can be constructed using semi-analytical techniques. The dam-break initial conditions engender self-similar flow profiles expanding at a constant rate, which can be integrated to arbitrary accuracy using simple

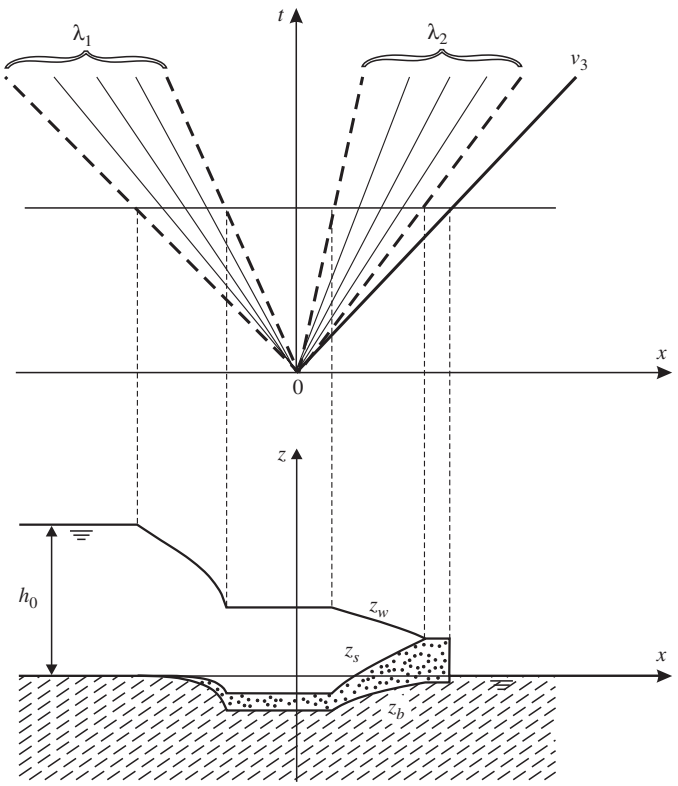

Figure 6. Semi-analytical solution to the erosional dam-break problem. Top: wave structure; bottom: interface profiles. The self-similar solution features two inner constant states, two smooth rarefaction waves, and a discontinuous shock at the wavefront.

numerical quadrature. The resulting profiles and underlying wave structure are illustrated on Figure 6. Two inner constant states form at the centre and tip of the surge. Two rarefaction waves, or centred simple waves, extend upstream and downstream of the central constant state. Finally a discontinuous shock forms at the wave front, where the sediment transport layer invades the whole depth of the flow. As it progresses, the shock erodes material from the bed, hence the term 'erosional bore' used in Reference [19] to describe this feature. The solution represents a generalisation to erodible beds of the Stoker solution of pure water hydrodynamics [20]. It includes both weak and strong shocks which reflect the significant impact of erosional entrainment on the flow dynamics. The solution thus constitutes a challenging benchmark for the testing of numerical schemes.

4.2. Comparison of numerical and analytical results

We first compare numerical results with the semi-analytical solutions. For the purpose of this comparison, computations are performed for the two different density contrasts $s = \rho_s/\rho_w = 1.05$ and 1.5, with friction factor k set to zero. Figure 7 plots first order results obtained with the proposed LHLL method together with the Riemann semi-analytical profiles. A rather coarse

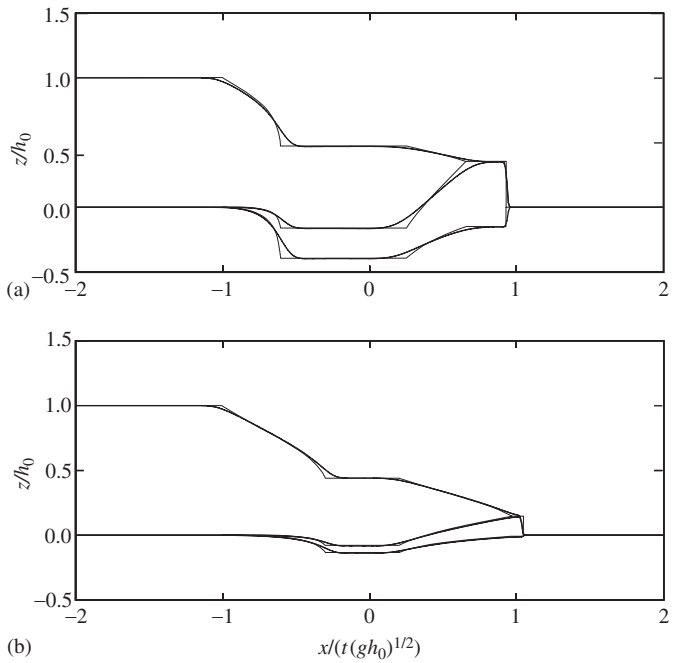

Figure 7. Results for the first-order accurate version of the proposed LHLL scheme, for materials of two different density ratios $s = \rho_s/\rho_w$: (a) $s = 1.05$; (b) $s = 1.5$. Thin lines = semi-analytical solution; thick lines = computational results. Spatial discretization $(th_0)/(t_0\Delta x) = 100$ (coarse grid).

discretization is chosen to facilitate assessment of the results. We set $(th_0)/(t_0\Delta x) = 100$, where h_0 is the initial water depth and $t_0 = (h_0/g)^{1/2}$ is the hydrodynamic time scale. The comparison is satisfactory for all three interfaces z_w, z_s and z_b. The levels in the constant state regions are well-predicted, and the solutions well-behaved. In particular, the scheme successfully handles the erosional shock at the wave front. The sharp angles of the Riemann solutions are however significantly blunted in the numerical profiles, reflecting the diffusive nature of the HLL flux function. Figure 8 provides the corresponding plots for the alternative CLF scheme. Results of good quality are also obtained, with accurate levels obtained for the constant states. Comparison of Figures 7 and 8, however, shows that the CLF scheme is even more diffusive than the proposed LHLL method: differences are apparent especially at the corners where simple waves connect with the inner constant states. The more diffusive behaviour of the CLF scheme is directly related to the use of the Lax-Friedrichs rather than HLL flux function.

Figure 9 plots results in the same conditions as Figure 8, but computed with the second-order version of the LHLL scheme. The results show significant improvement. Numerical diffusion is considerably reduced, and the resolution of the various waves is enhanced. At the same time, the results remain non-oscillatory. The lateralised flux approach is therefore successful in preventing unphysical oscillations in the presence of the non-conservative bottom slope product. The second order extension also greatly speeds up convergence as the grid is refined. This is illustrated in Figure 10, where second-order LHLL computations are

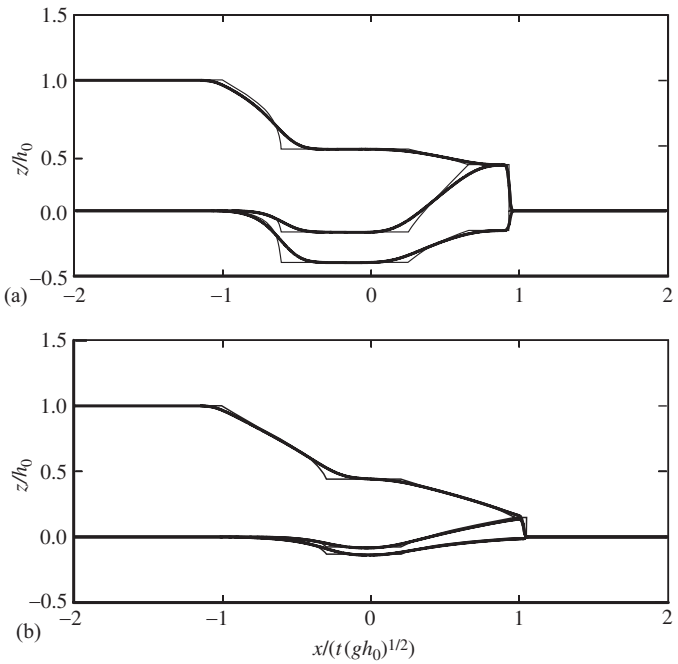

Figure 8. Results for the first-order accurate version of the CLF scheme chosen for comparison. Spatial discretization $(th_0)/(t_0\Delta x) = 100$ (coarse grid).

presented for a discretization $(th_0)/(t_0\Delta x) = 500$, which is only moderately finer than previously. Improvement is most dramatic in the wave front region of the flow over heavier sediment material (Figure 10(b)), where the scheme successfully resolves the delicate constant state region just upstream of the erosional shock. This is a feature which was significantly blurred in the results of Figures 7–9.

Corresponding results for the second-order version of the CLF scheme are virtually indistinguishable, as shown in Figure 11. This confirms the conclusion of Nujic [6] that using a more diffusive flux function does not matter so much when going to second-order accuracy. As shown by the details magnified in Figures 12(c), 12(d), however, small spikes are observed upstream of the discontinuous wave front, indicating that the CLF strategy is mostly but not entirely successful at preventing oscillatory behaviour. The proposed LHLL scheme performs better in this regard, as seen in Figures 12(a), 12(b).

4.3. Comparison of numerical and experimental results

To convey qualitatively the behaviour of erosional dam-break flows, Figure 13 reproduces experimental images from Reference [17]. On the digital photos, white granular particles contrast with the dark water against a gray backdrop grid. The images show how the surge quickly evolves into what is essentially a shallow water wave expanding at a constant rate. Entrainment of material is most severe at the centre of the wave, where a scour hole forms, and transport most intense at the wave front. The latter develops into a mature debris flow surge

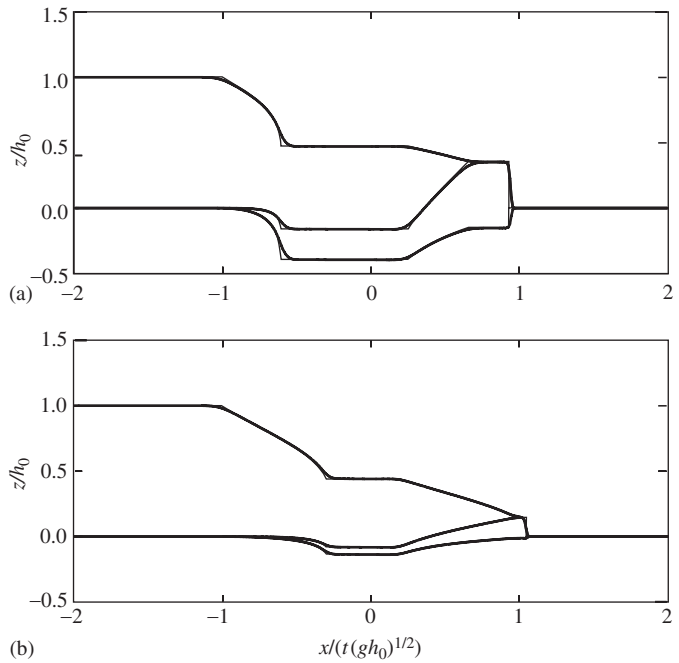

Figure 9. Results for the second-order accurate version of the proposed LHLL scheme. Spatial discretization $(th_0)/(t_0\Delta x) = 100$ (coarse grid).

in which the transport layer invades the entire flow depth, with a steep shock-like snout. One feature which is missed by the present description is the hydraulic jump which breaks at the wave centre. This is likely due to non-equilibrium and non-hydrostatic effects, which require a more complete description than the present equilibrium shallow water theory [14]. Overall, however, the qualitative behaviour matches well the semi-analytical and computational results presented in the previous section.

The numerical results can now be compared with the measured interface profiles. Using the computational scheme proposed above, frictional momentum losses can be included. Their effects on the flow can therefore be examined quantitatively, something which could not be done using the Riemann semi-analytical solution. Results for the Taipei light grain experiments are plotted in Figure 14, and corresponding results for the Louvain experiments are shown in Figure 15. While the flow pattern is similar for the two tests, the sediment entrainment is considerably less severe in the Louvain experiments due to the heavier sediment material used. In both cases, the quantitative comparison for all three interfaces z_w, z_s and z_b is quite favourable. The contrast between light and dense sediment materials furthermore appears to be well-captured by the theory. Note that this agreement is achieved using non-dimensional entrainment coefficient C_f as the sole adjustable parameter, with the same calibrated value $C_f = 0.014$ chosen for both series of tests.

A lesson of particular interest concerns frictional momentum losses. The relevant source term is included in the two series of computations. In both cases, the value $\tan\varphi = 0.5$ documented in the literature was used for the frictional parameter, hence no *ad hoc* calibration is

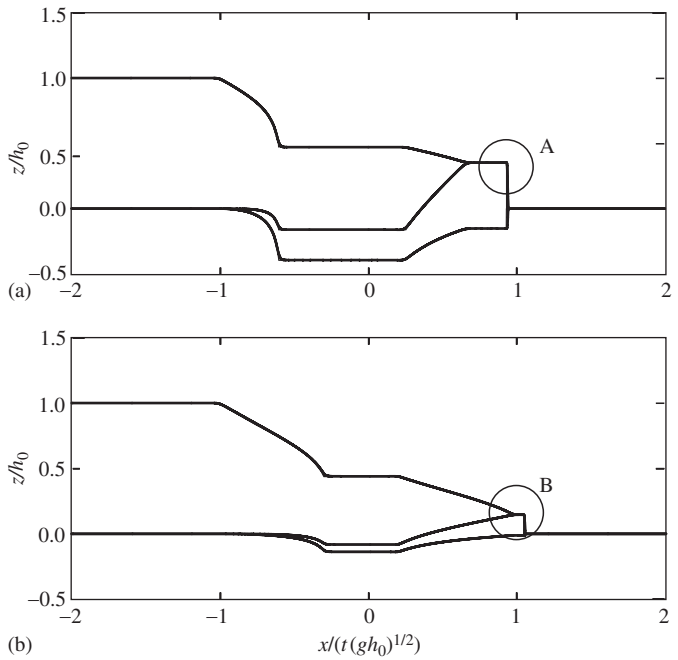

Figure 10. Results for a finer grid having spatial discretization $(th_0)/(t_0\Delta x) = 500$. Second-order accurate version of the proposed LHLL scheme.

involved. For the light grain Taipei tests, frictional effects turn out to be negligible, and the solutions remain indistinguishable from the frictionless computations. This appears in agreement with the experimental observations. For the Louvain tests, on the other hand, the effects are more apparent. This is highlighted in Figure 15(d) by plotting the 'frictionless' Riemann solution together with the 'frictional' computations. As a result of the significant non-homogeneous term, the numerical profiles are no longer entirely self-similar. The 'frictional' computations are further seen to be consistent with the experimental profiles, providing a better agreement than the 'frictionless' semi-analytical results.

While the trends go in the right direction, frictional effect appear to be felt slightly more strongly in the experiments, as indicated by the shape adopted by the bed profile z_b in Figure 15. This discrepancy is probably due to our assumption of perfect velocity coupling between the pure water and sediment transport layers. In reality, the two layers are only partly coupled. It is therefore logical that bed friction influences more strongly the sediment layer, on which it acts directly, than the pure water layer on which it acts indirectly. In Reference [19], two conclusions were drawn from a theoretical time scale analysis. First, frictional momentum losses were expected to have only a weak effect on the flow in the initial stages of wave development. Secondly, a stronger impact was predicted for dense sediments than for light granular materials. The present comparison of experimental and computational results provides quantitative evidence in support of both these conclusions.

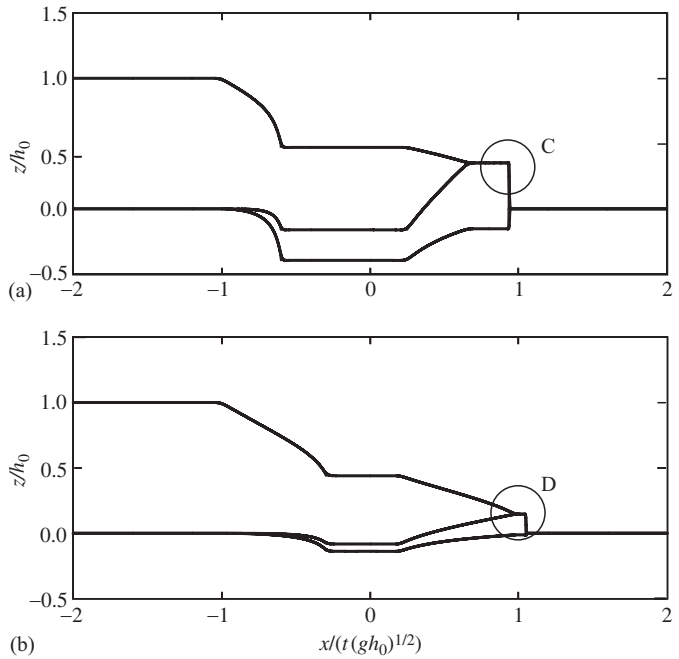

Figure 11. Corresponding computations for the second-order accurate version of the alternative CLF scheme. Spatial discretization $(th_0)/(t_0\Delta x) = 500$ (finer grid).

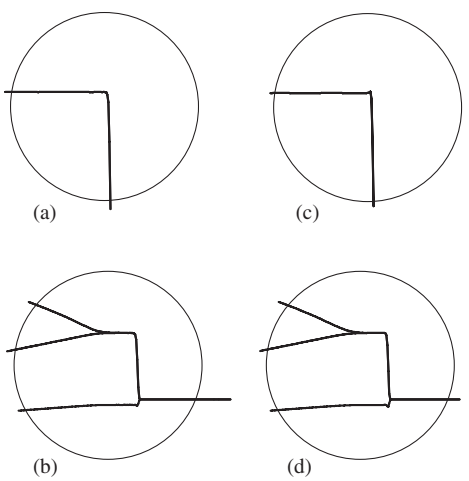

Figure 12. Details of the regions circled in Figures 10 and 11: (a), (b) regions A and B for the proposed LHLL scheme; (c), (d) regions C and D for the alternative CLF scheme. Second-order version of both schemes with spatial discretization $(th_0)/(t_0\Delta x) = 500$ (finer grid).

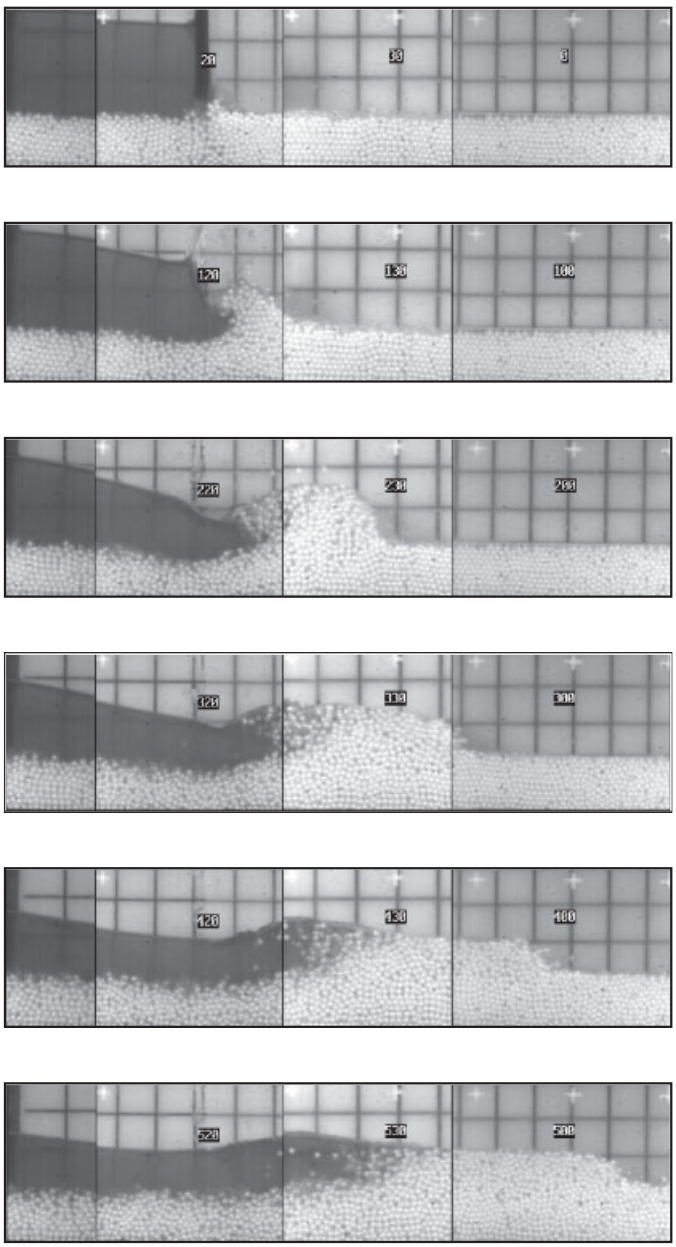

Figure 13. Image mosaics for the Taipei erosional dam-break wave experiments. The instants selected are, from top to bottom: $t = 0$, $t = t_0$, $t = 2t_0$, $t = 3t_0$, $t = 4t_0$, and $t = 5t_0$, where $t_0 = (h_0/g)^{1/2}$ and $h_0 = 10$ cm is the initial water depth (digital footage from Reference [17]).

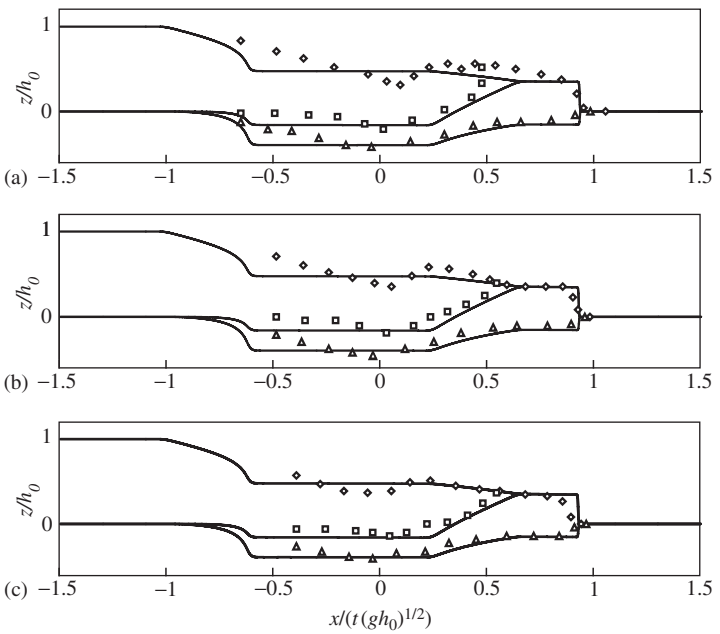

Figure 14. Comparison of experimental and numerical results (with frictional momentum losses) for the Taipei light sediment tests ($s = 1.048$): (a) $t/t_0 = 3$; (b) $t/t_0 = 4$; (c) $t/t_0 = 5$. Symbols = experimental measurements; diamonds = flow free surface z_w; squares = boundary between clear water and sediment transport layers z_s; triangles = bottom profile z_b; solid lines = computed profiles. LHLL second order with $(th_0)/(t_0\Delta x) = 500$. Experimental data from Reference [19].

5. CONCLUSIONS

The present paper documents a Godunov-type scheme developed for the computation of erosional shallow water transients. Based on a sharp interface view of the vertical flow structure, the adopted governing equations prove simple enough for numerical treatment yet appear sufficiently complete to capture essential features of the flow physics. The computational approach uses the HLL scheme as a basic building block, treats the bottom slope by lateralizing the momentum flux, then refines the scheme using Strang splitting and MUSCL extrapolation. Second order accuracy is achieved in smooth regions of the flow and oscillation-free behaviour at localized discontinuities. Thanks to the lateralized flux treatment, this property of the MUSCL approach carries over from the fully conservative case to the present case featuring a non-conservative product. The lateralized flux strategy performs slightly better than an alternative central difference treatment proposed earlier for shallow water flows over rigid beds. The proposed LHLL is both less diffusive and more successful at preventing oscillatory behaviour than the CLF scheme. Excellent agreement is recorded between computations and semi-analytical Riemann solutions. Some of the more delicate features of the latter are observed to require second-order accuracy to be adequately resolved on moderately fine grids. Finally, the numerical results compare well with experimental measurements of erosional dam-break waves. The computations allow a quantitative assessment of the effects

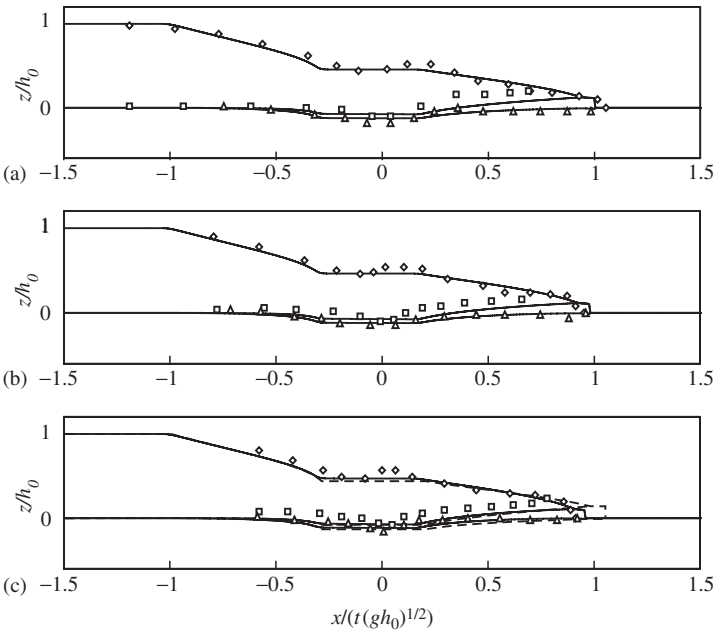

Figure 15. Comparison of experimental and numerical results (with frictional momentum losses) for the Louvain medium density sediment tests ($s = 1.54$): (a) $t/t_0 = 5$; (b) $t/t_0 = 7.5$; (c) $t/t_0 = 10$. Symbols and computational parameters as in Figure 14. Dashed lines on panel (c) are the frictionless semi-analytical profiles. Experimental data from Reference [19].

of frictional momentum loss on the wave development. The present framework, however, does not account for other physical effects which may play a significant role in certain circumstances. These include non-equilibrium transport, non-hydrostatic pressure, and slip between pure water and sediment transport layers.

REFERENCES

1. Fennema RJ, Chaudhry MH. Simulation of one-dimensional dam-break flows. *Journal of Hydraulic Research* 1987; **25**:41–51.
2. Glaister P. Approximate Riemann solutions of the shallow water equations. *Journal of Hydraulic Research* 1988; **26**:293–306.
3. Toro EF. Riemann problems and the WAF method for solving the two-dimensional shallow water equations. *Philosophical Transactions of the Royal Society of London* A 1992; **338**:43–68.
4. Alcrudo F, Garcia-Navarro P. A high resolution Godunov-type scheme in finite volumes for the 2D shallow water equations. *International Journal of Numerical Methods in Fluids* 1993; **16**:489–505.
5. Bermudez A, Vazquez ME. Upwind methods for hyperbolic conservation laws with source terms. *Computers and Fluids* 1994; **23**:1049–1071.
6. Nujic M. Efficient implementation of non-oscillatory schemes for the computation of free-surface flows. *Journal of Hydraulic Research* 1995; **33**:101–111.
7. Laigle D, Coussot P. Numerical modeling of mudflows. *Journal of Hydraulic Engineering* 1997; **123**:617–623.
8. Ming J, Fread DL. 1D modeling of mud/debris unsteady flows. *Journal of Hydraulic Engineering* 1999; **125**:827–834.
9. Armanini A, Di Silvio G. A one-dimensional model for the transport of a sediment mixture in non-equilibrium conditions. *Journal of Hydraulic Research* 1988; **26**:275–292.

10. Lai C. Modelling alluvial channel flow by multimode characteristic method. *Journal of Hydraulic Engineering* 1991; **117**:32–53.
11. Lapointe MF, Secretan Y, Driscoll SN, Bergeron N, and Leclerc M. Response of the Ha! Ha! River to the flood of July 1996 in the Saguenay Region of Quebec: Large-scale avulsion in a glaciated valley. *Water Resources Research* 1998; **34**:2383–2392.
12. Takahashi T. *Debris Flow*. IAHR Monograph. Balkema: Amsterdam, 1991.
13. Asano T. Sediment transport under sheet-flow conditions. *Journal of Waterway, Port, Coastal and Ocean Engineering* 1995; **121**:239–246.
14. Capart H, Young DL. Formation of a jump by the dam-break wave over a granular bed. *Journal of Fluid Mechanics* 1998; **372**:165–187.
15. Takahashi T, Nakagawa H. Flood/debris flow hydrograph due to the collapse of a natural dam by overtopping. *JSCE Journal of Hydroscience and Hydraulic Engineering* 1994; **12**:41–49.
16. Hungr O. A model for the runout analysis of rapid flow slides, debris flows, and avalanches. *Canadian Geotechnical Journal* 1995; **32**:610–623.
17. Capart H. Dam-break induced geomorphic flows and the transition from solid- to fluid-like behaviour across evolving interfaces. *PhD Thesis*, Univ. catholique de Louvain, 2000.
18. Fraccarollo L, Armanini A. A semi-analytical solution for the dam-break problem over a movable bed. *Proceedings of the 28th IAHR Congress*, Graz, 1999; 381.
19. Fraccarollo L, Capart H. Riemann wave description of erosional dam-break flows. *Journal of Fluid Mechanics* 2002; **461**:183–228.
20. Stoker JJ. *Water Waves*. Interscience Publishers. Wiley: New York, 1957.
21. Roe PL. Approximate Riemann solvers, parameter vectors and difference schemes. *Journal of Computational Physics* 1981; **43**:357–372.
22. Leveque RJ. Balancing source terms and flux gradients in high-resolution Godunov methods: the quasi-steady wave-propagation algorithm. *Journal of Computational Physics* 1998; **146**:346–365.
23. Bereux F, Sainsaulieu L. A roe-type Riemann solver for hyperbolic systems with relaxation based on time-dependent wave decomposition. *Numerische Mathematik* 1997; **77**:143–185.
24. Saurel R, Abgrall R. A multiphase Godunov method for compressible multifluid and multiphase flows. *Journal of Computational Physics* 1999; **150**:425–467.
25. Harten A, Lax PD, Van Leer B. On upstream differencing and Godunov-type schemes for hyperbolic conservation laws. *SIAM Review* 1983; **25**:35–61.
26. Sillen X. Ecoulements transitoires à surface libre: modéles numériques et physiques. *PhD Thesis*, Univ. catholique de Louvain, in preparation.
27. Capart H, Eldho TI, Huang SY, Young DL, Zech Y. Treatment of natural topography in finite volume computations of open-channel flow. *Journal of Hydraulic Engineering* 2003; in press.
28. Strang G. On the construction and comparison of difference schemes. *SIAM Journal on Numerical Analysis* 1968; **5**:506–517.
29. Van Leer B. Toward the ultimate conservative difference scheme. III. Upstream-centered finite-difference schemes for ideal compressible flows. *Journal of Computational Physics* 1977; **23**:263–275.
30. Jenkins JT, Askari E. Boundary conditions for rapid granular flows: phase interfaces. *Journal of Fluid Mechanics* 1991; **223**:497–508.
31. Abbott MB. *Computational Hydraulics. Elements of the Theory of Free Surface Flows.* Pitman: London, 1979.
32. Castro M, Macias J, Pares C. A *Q*-scheme for a class of systems of coupled conservation laws with source term. Application to a two-layer 1-D shallow water system. *Mathematical Modelling and Numerical Analysis* 2001; **35**:107–127.
33. Capart H, Young DL. Two-layer shallow water computations of torrential geomorphic flows. *Proceedings of the International Conference on Fluvial Hydraulics*. Louvain-la-Neuve, 2002; 1003–1012.
34. Nnadi FN, Wilson KC. Motion of contact-load particles at high shear stress. *Journal of Hydraulic Engineering* 1992; **118**:1670–1684.
35. Fiedler FR, Ramirez JA. A numerical method for simulating discontinuous shallow flow over an infiltrating surface. *International Journal for Numerical Methods in Fluids* 2000; **32**:219–240.
36. Spiegel MR, Liu J. *Mathematical Handbook of Formulas and Tables*. McGraw-Hill: New York, 1999.
37. Golub GH, Van Loan CF. *Matrix Computations*. J. Hopkins Univ. Press, 1983.
38. Fraccarollo L, Toro EF. Experimental and numerical assessment of the shallow water model for two-dimensional dam-break type problems. *Journal of Hydraulic Research* 1995; **33**:843–864.
39. Toro EF. *Riemann Solvers and Numerical Methods for Fluid Dynamics*. Springer: Berlin, 1997.
40. Tseng MH, Hsu CA, Chu CR. Channel routing in open-channel flows with surges. *Journal of Hydraulic Engineering* 2001; **127**:115–122.
41. Van Goethem JL, Villers L. Modélisation du transport solide associé à l'onde de rupture d'un barrage. *BEng Thesis*, Univ. catholique de Louvain, 2000; 152–161.

